Supplemental Information

Numerical simulation of parallel-plate particle separator for estimation of charge distribution of PM2.5

Takuto Yonemichi[a], Koji Fukagata[a], Kentaro Fujioka[b], and Tomoaki Okuda[b]

[a]Department of Mechanical Engineering, Keio University, 3-14-1 Hiyoshi, Kohoku-ku, Yokohama, Japan;
[b]Department of Applied Chemistry, Keio University, 3-14-1 Hiyoshi, Kohoku-ku, Yokohama, Japan.

S1.   Experimental setup

Here, we briefly overview the experimental setup used in our experiment (Okuda, Gunji, and Lenggoro, 2015), since the information is not available in literature written in English.

Figure S1 shows the schematic of the inlet section of the PPPS used in our experiment, including the region outside of the computational domain of the present simulation. Aerosol and sheath air flow are introduced from the pipes connected vertically to the channels at the center of the z-direction. Note that the exit section has the same configuration as the inlet section.

Figure S2 shows the schematic of the experimental setup to investigate the relationship between flow ratio, F_R, and the collection ratio, C_R. An air flow of 1.5 L/min in total was introduced by three pumps of optical particle counters (OPCs, Rion KC-01D and KC01-E) with a flow rate of 0.5 L/min each installed in the downstream of the exit channels. The flow rates of the inlet sections were controlled by valves and mass rotameters (KOFLOC RK-1450). The aerosol of standard polystyrene particles was generated by spraying with an atomizer (TSI Model 3079) and a dryer. The aerosol was introduced to Inlet 2, and sheath air flowed through PTEE filters (Millipore Millex-FA) was introduced to Inlets 1 and 3. The number of particles flowing out to each exit was counted by the OPC.

S2.   Verification of the numerical simulation

For the verification of the numerical integration of the particle equation of motion and the model of Brownian diffusion, trajectories of 200,000 particles injected from the point source $(x,\ y) = (0,\ 0)$ are computed in a uniform flow field. Figure S3 shows the time trace of variance of the particle position y_p, i.e., $\sigma^2(y_p)$, with that of the exact solution, given by

$$\sigma^2(y_p) = \frac{2t}{\mathrm{Re}_h \mathrm{Sc}}. \tag{S1}$$

It is found that the residual of the variance with $\Delta t = 1 \times 10^{-3}$ with respect to that with $\Delta t = 1 \times 10^{-4}$ is less than 1% in the time of $t \geq 100$. Further, it is confirmed that the variance with $\Delta t = 1 \times 10^{-3}$ is in good agreement with that of exact solution: the error is less than 2%. Note that the error is larger than that estimated from Chebyshev inequality (Buslenko et al. 1966) for 200,000
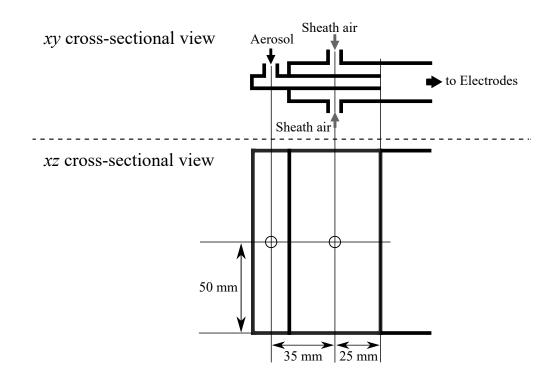

Figure S1. Schematic of the inlet section redrawn based on the figure of Okuda, Gunji, and Lenggoro (2015).
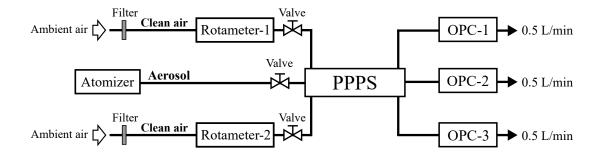
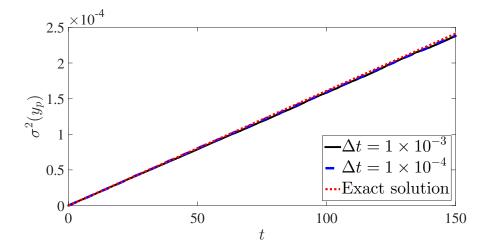**Figure S2.** Schematic of the experimental setup.

Figure S3. Time trace of $\sigma^2(y_p)$ (i.e., the variance of y_p) calculated using 200,000 Brownian particles injected from a point source in a uniform flow field.

particles. In the present simulation, however, we have judged that the time step is sufficiently small because it has been confirmed that the error of the variance of 2% has negligible effect on the resultant collection ratio (0.16% error on $C_{R,2}$), which is central to the present discussion.

S3. Complementary Results and Discussion

S3.1. *Cases without electric field*

Figure S4 shows the streamlines and trajectories of 50 particles chosen at random in Case 100. The color of the streamlines represents the value of the stream function. It has been confirmed, by monitoring the temporal evolution of the pressure drop and local velocities at different locations, that the obtained flow field is steady and symmetric with respect to the x-axis. The particle trajectories approximately coincide with the streamlines. However, some particles are observed to flow out to Exits 1 and 3 despite the fact that all the streamlines from Inlet 2 are connected to Exit 2. It is noticed from Figure S4(a) that the particles flowed out to the unexpected exits (i.e. Exits 1 and 3) are those close to the walls of Inlet 2. This observation suggests that the device performance can be improved by altering the trajectories of such particles.

In order to evaluate the performance improvement relative to Case 100, we define the improvement ratio, $I_{R,i}$, as

$$I_{R,i} = \left[1 - \frac{1 - C_{R,i}}{1 - C_{R,i}^0} \right] \times 100\%, \tag{S2}$$

where the superscript $(\cdot)^0$ denotes the value in Case 100.

Figure S5 shows $I_{R,2}$ in Case CW and Case SW as a function of $W_{IC,2}$. It is found that $I_{R,2}$ increases as $W_{IC,2}$ decreases, and that the $I_{R,2}$ values of these two cases are similar to each other. An approximately 50% improvement is achieved in Case CW025 and in Case SW175.

Figure S6 shows sample particle trajectories in Case U078, Case 100, and Case U120. With decreasing F_R, the particle trajectories shift inward following the contraction of streamlines (see also Figure S7). Consequently, particle trajectories are more focused toward the desirable exit.

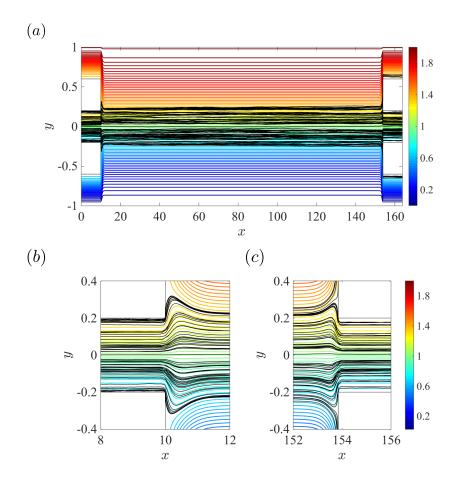Figure S7 shows wall-normal velocity v_f around the entrance of the classification section, i.e.,

3

Figure S4. Streamlines and particle trajectories of 50 particles in Case 100: (a) overview; (b) upstream side of the classification section; (c) downstream side of the classification section. Colored line, streamlines; black line, particle trajectories.
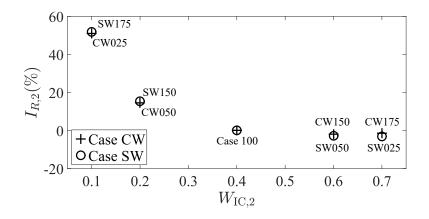

Figure S5. Improvement ratio ($I_{R,2}$) in Case CW and Case SW as a function of the width of Inlet 2 ($W_{\mathrm{IC},2}$).
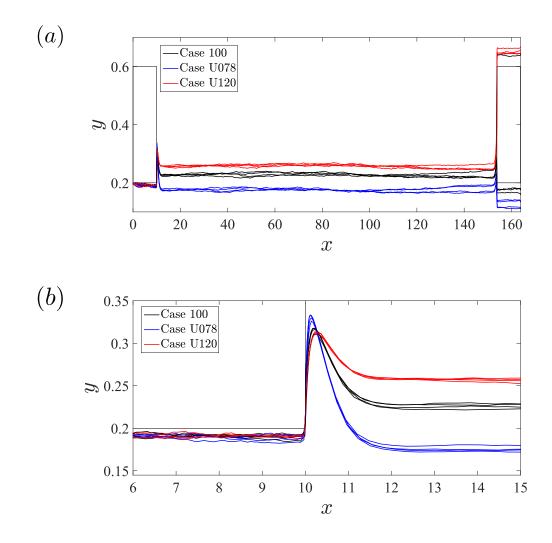
Figure S6. Sample trajectories of four particles close to the upper wall of Inlet 2: (*a*) overview; (*b*) zoom-up view of the upstream side of the classification section.
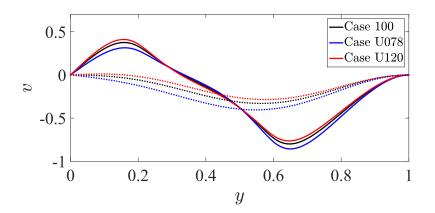
Figure S7. Wall-normal velocity of fluid v_f in Case U078, Case U120, and Case 100. Dotted line, at $x = 10.12$; solid line, at $x = 10.60$.
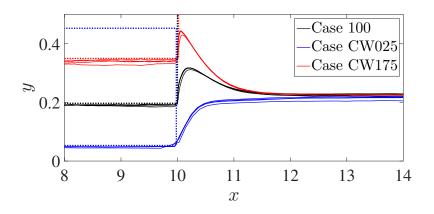

Figure S8. Sample trajectories of four particles around the entrance of the classification section in Case CW025, Case CW175, and Case 100. Dotted line shows the position of the separator in the inlet section in each case.

$x = 10.12$ and $x = 10.6$. It is found that, by decreasing F_R, a flow is induced toward the center of the device. Because particles basically flow along the streamlines, this induced flow transports particles toward the center of the device.

Figure S8 shows sample trajectories of the particles which are close to the upper wall of Inlet 2 around the entrance of the classification section in Case CW025, Case CW175 and Case 100. The dotted line in Figure S8 shows the position of the separator in each case. It is observed that the trajectories slightly shift toward the center of the device with decreasing $W_{\mathrm{IC},2}$. Note that the modification of trajectories in Case SW is similar to that of Case CW at corresponding $W_{\mathrm{IC},2}$. Namely, narrowing $W_{\mathrm{IC},2}$ has the same effect, i.e., bringing particles toward the center of the device as decreasing F_R.

S3.2. *Cases with electric field*

Figure S9 shows the distribution of the non-dimensional electric potential Φ in the computational domain. It is confirmed that the electric field between the electrodes is uniform in the x-direction. It is also confirmed that the electric field in the inlet section and exit section is negligibly small.
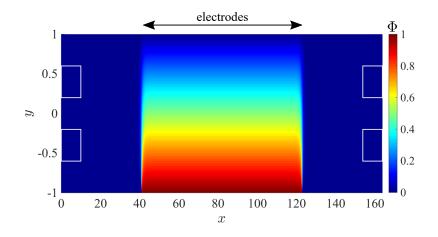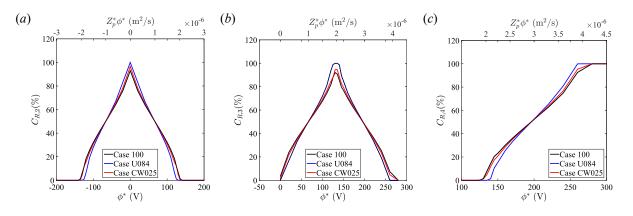
Figure S9. Distribution of the non-dimensional electric potential Φ. the positive electrode is at $40.96 \leq x \leq 122.88$, $y = -1.00$, and the negative electrode is at $40.96 \leq x \leq 122.88$, $y = 1.00$.

Figure S10. Collection ratio (C_R) as a function of applied voltage (ϕ^*) and the electrical mobility (Z_p^*) in Case 100, Case U084 and Case CW025: (*a*) Exit 2; (*b*) Exit 3; (*c*) the upper wall.

Figure S10 shows the collection ratio, C_R, as a function of applied voltage, ϕ^*, and the electrical mobility, Z_p^*, in Case 100, Case U084 and Case CW025. In regard to the collection ratio of Exit 3, $C_{R,3}$ is substantially higher in Case U084 and Case CW025 than in Case 100. In particular, $C_{R,3}$ in Case U084 is the highest under the applied voltage of 70 V $\leq \phi^* \leq$ 195 V, and $C_{R,3} > 99\%$ under the applied voltage of $\phi^* = 130$ V and $\phi^* = 135$ V.

Figure S11 shows the improvement ratio of Exit 3, $I_{R,3}$, based on the results of Case 100 at the corresponding applied voltage. The dotted lines show $I_{R,2}$ in Case U084 and Case CW025 without an applied voltage. In the Case U084, $I_{R,3}$ reaches $I_{R,3} = 100\%$ with $\phi^* = 135$ V, and in the Case CW025, it reaches $I_{R,3} = 42.23\%$ with $\phi^* = 135$ V. The tendency is similar to that of $I_{R,2}$ without applying the voltage. Again, $I_{R,3}$ gradually decreases as ϕ^* deviates from 135 V.

Figure S12 shows the trajectories of 100 charged particles under $\phi^* = 135$ V in Case 100 and Case U084. At the entrance of the classification section, the particle trajectories in Case U084 are focused similarly to those in the absence of an electric field (Figure S6) so as to be directed toward the desired exit. Therefore, the strategy to improve the classification accuracy by adjusting the inlet flow rate or width is also valid under the presence of an electric field, although the value of I_R varies depending on the applied voltage.
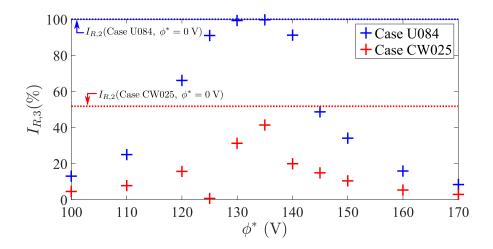
7

Figure S11. Improvement ratio of Exit 3, $I_{R,3}$, as a function of applied voltage, ϕ^*.

Table S1. Numerical conditions and collection ratio for additional cases.

Case	Numerical conditions		Collection ratio(%)		
	$U_{I,1} : U_{I,2} : U_{I,3}$	Initial distribution	$C_{R,1}$	$C_{R,2}$	$C_{R,3}$
Case 100 (simulation)	$1 : 1 : 1$	Uniform distribution	3.67	92.65	3.68
Case 100 (experiment)	$1 : 1 : 1 \ (\pm 3\%)$	Unknown	6.8	80.3	12.9
Case AS1	$1 : 1 : 0.97$	Uniform distribution	2.34	90.58	7.08
Case AS2	$1 : 1 : 1$	Asymmetry (Equation S3)	1.69	91.55	6.76
Case AS3	$0.96 : 1 : 1$	Asymmetry (Equation S3)	4.62	91.37	4.01

S3.3. *Discussion on the difference between numerical and experimental results*

The reason for the difference observed in Figure 3 may be three-fold: (1) measurement error of the flow rate in each channel of the inlet section; (2) error in geometry due to insufficient assembling accuracy of the PPPS; (3) nonuniform particle distribution at Inlet 2. To elucidate the reason, we numerically reproduce such inaccurate conditions and compute the trajectories of particles. The measurement error of the flow rate is set 3% following the accuracy of the rotameter used in the experiments. The error of the geometry in the y-direction between the blueprint and the actual device is set 25% of the width of the paths in the inlet section (0.25 mm) considering that the PPPS is assembled by hand. The nonuniform distribution in the y-direction of particles are made by the rejection method (Press et al., 1992), using the PDF as

$$p(y) = \begin{cases} \frac{25}{6}y + \frac{5}{2} & (-0.2 \leq y \leq 0.2), \\ 0 & (\text{otherwise}). \end{cases} \tag{S3}$$

It is found that the error in geometry has negligible effect on the distribution of particles at the exit section: the collection ratio in this case is in the range of the standard deviation of Case 100. On the other hand, the remaining two factors are found to have impact on C_R and the distribution of particles in the exit section. The numerical conditions and the C_R of those cases are shown in Table S1. By focusing on Exit 2, it is revealed that $C_{R,2}$ of Case AS1 and that of Case AS2 are smaller than that of Case 100 considering the standard deviation of $C_{R,2}$ shown in Table 2, and these are closer to the experimental results. Furthermore, by focusing on Exits 1 and 3, $C_{R,3}$ is more than three times greater than $C_{R,1}$ in both cases. In Case AS1, the wall-normal fluid velocity v_f at the entrance of the classification section (i.e., $x = 10.12,\ 10.60$) is larger than that in Case
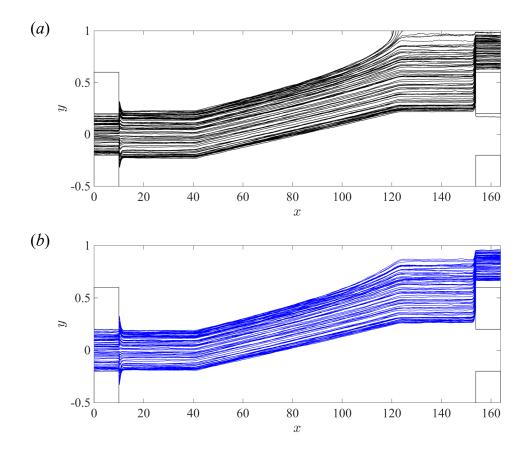
Figure S12. Trajectories of 100 particles charged $N_c = 4$ with the applied voltage of $\phi^* = 135$ V: (*a*) Case 100; (*b*) Case U084.

100. Because the flow in this region transports particles toward the upper wall, $C_{R,1}$ in Case AS1 becomes lower and $C_{R,3}$ becomes larger than those in Case 100. In Case AS2, the distribution initially biased to Exit 3 side, as shown in Figure S13(*b*), remains biased at the exit, $x = 163.84$.

Figure S13 also shows an important suggestion that the difference between $C_{R,1}$ and $C_{R,3}$ can be suppressed by controlling the flow rates of the inlet paths in experiments. In Case AS3, the flow field that causes particles to tend to flow out to Exit 1 is induced by the balance of bulk-mean velocities U_I. On the other hand, the initial distribution of particles biases to the side of Exit 3. As a result, the difference between $C_{R,1}$ and $C_{R,3}$ becomes smaller compared to that of Case AS2.

S3.4. *Discussion on the accuracy of the determined charge distribution*

We perform the test shown in Section 5.2 under various conditions in order to obtain a more accurate result and to confirm the reproducibility of the proposed method in experiments. The test cases are listed in Table S2. Both the flow field and set of the applied voltages are chosen as unoptimized cases (Case 100, $\phi^* = 100, 135, 200, 300$, and 400 V) and the optimized ones (Case U084, $\phi^* = 108, 135, 180, 270$, and 540 V) based on the results of the numerical simulation.

Figure S14 shows the sum of the residuals, R_{sum}, calculated as

$$R_{\text{sum}} = \sum_{i=-5}^{5} R^i, \tag{S4}$$
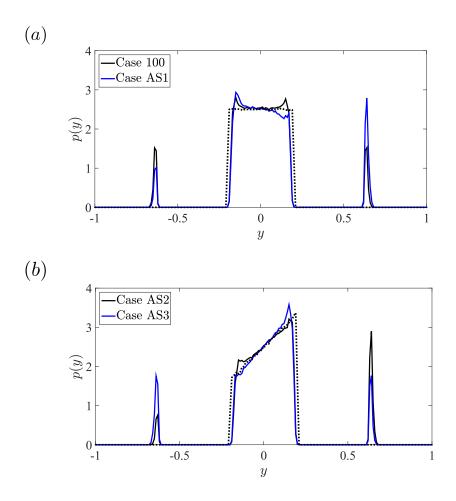
9

(a)

(b)

Figure S13. Probability density function of the particles at $x = 163.84$ with an asymmetric initial distribution of particles given by Equation (S3). Dotted line shows the initial distribution of particles.

as a function of the determinant of the matrix of the collection ratio, $\det(C_R)$. It is found that R_{sum} becomes the smallest in Case CD4, i.e., the case using optimized conditions. The strategy to improve the classification accuracy discussed in Section 4 is therefore valid also under such practical situation. In addition, a tendency that R_{sum} decreases with increasing $\det(C_R)$ is observed. The reason for this tendency is explained by propagation of the errors in the number of particles counted at the exit channels. Assuming that the errors included in the number of particles are identical in all cases, the errors of the determined charge distribution becomes smaller when the size of the inverse of C_R is smaller. Because the magnitude of the inverse matrix is small when the determinant of the matrix is large, R_{sum} decreases as increasing $\det(C_R)$.

From the viewpoint of the reproducibility, the influence of the significant figures on the estimation accuracy is investigated. Figure S15 shows R_{sum} computed with different significant figures.

Table S2. Numerical conditions for determining charge distribution.

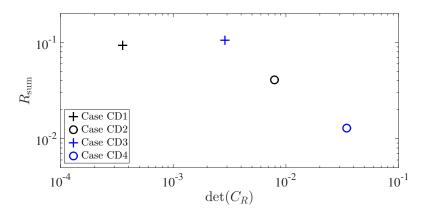| Case	Flow field	Applied voltages
Case CD1	Case 100	$100, 135, 200, 300, 400$ V
Case CD2	Case 100	$108, 135, 180, 270, 540$ V
Case CD3	Case U084	$100, 135, 200, 300, 400$ V
Case CD4	Case U084	$108, 135, 180, 270, 540$ V

Figure S14. Sum of the residuals, R_{sum}, as a function of the determinant of the matrix of the collection ratio, $\det(C_R)$.
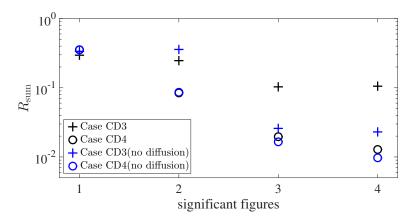

Figure S15. Sum of the residuals, R_{sum}, as a function of the significant figures for the computation of the charge distribution of particles.

It is found that the estimation accuracy rapidly decreases with decreasing the significant figures due to increment of the rounding error. However, R_{sum} of Case CD4 with the significant figures of two digits, i.e., a reproducible condition in experiments, indicates an allowable value, and the determined distribution maintains that of the input as shown in Figure S16. Thus, the proposed method is valid for determining the charge distribution of aerosol particles in experiments.

Figure S15 also indicates that Brownian diffusion makes the estimation accuracy worse. The adverse effect of the Brownian diffusion becomes relatively unremarkable for the significant figures of less than three digits.
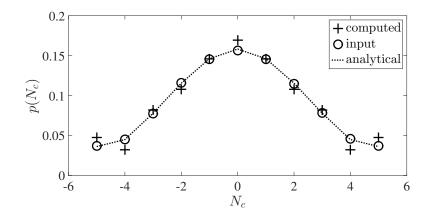
Figure S16. Charge distribution of particles computed from the number of particles classified by the PPPS in Case CD4 with significant figures of two digits.

References

Buslenko, N. P., D. I. Golenko, Yu. A. Shreider, I. M. Sobal, and V. G. Sragovich 1966. *The Monte Carlo method The method of statistical trials (English edition, Shreider, Yu. A. Ed.).* New York: Pergamon Press.

Okuda, T., Y. Gunji, and I. W. Lenggoro. 2015. Measurement of the electrostatic charging state of individual particles in ambient aerosol using Kelvin Probe Force Microscopy. *Earozoru Kenkyu* 30 (3):190–197. doi:10.11203/jar.30.190. (in Japanese)

Press, W. H., B. P. Flannery, S. A. Teukolsky, and W. T. Vetterling. 1992. *Numerical recipes in Fortran 77: The art of scientific computing.* New York: Cambridge University Press.